Chemically Non-Equilibrium Modeling of Argon Inductively Coupled Thermal Plasma with C-H-O Systems

Sharif Abdullah Al-MAMUN, Yasunori TANAKA
and Yoshihiko UESUGI

Division of Electrical Engineering & Computer Science
Kanazawa University, Kanazawa 920-1192, Japan

(Received: 4 September 2008 / Accepted: 12 November 2008)

In this work, a two-dimensional chemically non-equilibrium (NCE) model has been developed for Ar inductively coupled thermal plasma (ICTP) with C-H-O system at atmospheric pressure from the viewpoint of plasma process and fuel combustion. Chemically non-equilibrium effects have been taken into account by solving mass conservation equations for each of 22 particles (including atoms, molecules, ions and electrons) considering convection, diffusion and net production effects. For the net production term, totally 198 chemical reactions were taken into account including dissociation, ionization and other chemical reactions and their backward reactions.

Keywords: equilibrium composition, ICTP, C-H-O system, 1T-CE, 1T-NCE

1. Introduction

Nowadays, much attention has been paid to the plasma assisted combustion because the plasma can enhance, for example, the efficiency of the resultant combustion heat obtained due to high chemical reactivity [1]. It is very essential to understand not only the gas flow and temperature fields but also the inner chemistry of combustion reactions associated with all other reactions that may influence the combustion efficiency. Because it is thought to believe that plasma properties and combustion rates can be altered by controlling some reaction rates. To do this, active radicals or particle density should be investigated first. To know about the chemical fields such as spatial distribution of chemical species, CE modeling is not enough, NCE modeling is necessary instead.

In this paper, we have developed a two-dimensional chemically non-equilibrium model of Ar plasmas at atmospheric pressure with C-H-O molecular gas considering diffusion, convection and reaction rates for spatial distribution of chemical species [2]. Temperature, gas flow, and particle composition distributions were predicted by the developed model.

2. Dominant species and chemical reactions

2.1 Selection of reactions

To consider dominant particles in high power density Ar-$C_xH_yO_z$ molecular mixture plasma, equilibrium composition of Ar-$C_xH_yO_z$ system were calculated. For this calculation, all 53 chemical species in JANAF tables [3] were considered including Ar, C, H and O atoms. The equilibrium composition was calculated by minimization of Gibb's free energy. The temperature range was set to 300-30000 K. From the equilibrium composition, we found 22 dominant species such as CO_2, HO_2, O_2, O_2^+, CH_2O, CHO, CHO^+, CO, CO^+, H_2O, OH, O, O^+, CH_4, CH_3, H_2, H_2^+, H, H^+, Ar, Ar^+ and electron. These particles were selected for fluid dynamics modeling.

Among these species, there are numerous reactions. From literatures [4-15], totally 194 reactions that would be taken into account for a two-dimensional thermo-fluid dynamics modeling were selected as summarized in Tab.1. Reactions 29, 30, 33-37, 43-47, 50-52 include electrons, which may be related to the electrical conductivity of plasmas. Other reactions are positive or negative heat sources and radical sources.

2.2 Reaction rates

For selected reactions 1-28, we estimated reaction rates or obtained them from literatures [4]. Ionization reaction rates were calculated using an electron impact ionization cross-section (data collected from National Institute of Standards and Technology [5]) on the assumption of Maxwellian velocity distribution function for electrons. Fig.1 shows some of reaction rates as a function of heavy particle temperature. Reactions with the high frequency factor and low activation energy are dominant ones especially for high temperature region. Also, Fig.2 indicates some of electron impact ionization reaction rates as a function of electron temperature, which is also important in plasma-assisted combustion. Ionization reactions of H and O have comparatively higher rates than others and especially higher than Ar.

3. Chemically non-equilibrium modeling of high power density Ar- $C_xH_yO_z$ plasma at atmospheric pressure

3.1 Assumption

Using the estimation in the previous section, chemically non equilibrium modeling was made of high power density Ar- $C_xH_yO_z$ plasma at atmospheric pressure. In this work, following assumptions were taken for calculation [16]: (I) Each species has Maxwell-Boltzmann velocity

author's e-mail: 1202shar@ec.t.kanazawa-u.ac.jp

Tab.1. Reactions taken into account

Reactions		
(1) $H+HO_2 \rightarrow H_2+O_2$	(20) $CH_3+OH \rightarrow CH_2O+H_2$	(38) $H_2+O_2 \rightarrow 2OH$
(2) $H+HO_2 \rightarrow 2HO$	(21) $CH_2O+H \rightarrow CHO+H_2$	(39) $CO+O_2 \rightarrow CO_2+O$
(3) $H+HO_2 \rightarrow H_2O+O$	(22) $CH_2O+O \rightarrow CHO+OH$	(40) $CO+HO_2 \rightarrow CO_2+OH$
(4) $O+H_2 \rightarrow HO+H$	(23) $CH_2O+OH \rightarrow CHO+H_2O$	(41) $2CH_4+O_2 \rightarrow 2CO+4H_2$
(5) $O+HO_2 \rightarrow HO+O_2$	(24) $CHO+O \rightarrow CO+OH$	(42) $H_2+H \rightarrow H+H+H$
(6) $HO+H_2 \rightarrow H_2O+H$	(25) $CHO+H \rightarrow CO+H_2$	(43) $H+e \rightarrow H^++e+e$
(7) $HO+HO \rightarrow H_2O+O$	(26) $CHO+OH \rightarrow CO+H_2O$	(44) $H_2^++H_2+e \rightarrow H_2+H_2$
(8) $HO+HO_2 \rightarrow H_2O+O_2$	(27) $CHO+M \rightarrow CO+H+M$	(45) $H^++H_2+e \rightarrow H_2+H$
(9) $O+CH_3 \rightarrow HCHO+H$	(28) $CO+O+M \rightarrow CO_2+M$	(46 $H+H_2^++e \rightarrow H_2+H$
(10) $O+CH_4 \rightarrow HO+CH_3$	* 'M' means all the heavy particles considered;	(47) $H^++H+e \rightarrow H+H$
(11) $HO+CH_4 \rightarrow H_2O+CH_3$	(29) $Ar^++e+e \rightarrow Ar+e$	(48) $CH_3+H \rightarrow CH_4$
(12) $HO+CO \rightarrow H+CO_2$	(30) $Ar+Ar \rightarrow Ar^++e+Ar$	(49) $CH_4+O_2 \rightarrow CH_3+HO_2$
(13) $CHO+O_2 \rightarrow CO+HO_2$	(31) $O_2+O_2 \rightarrow O+O+O_2$	(50) $H_2+e \rightarrow H_2^++e+e$
(14) $H+O_2 \rightarrow OH+O$	(32) $O_2+O \rightarrow O+O+O$	(51) $CHO+e \rightarrow CHO^++e+e$
(15) $H+H+H_2 \rightarrow H_2+H_2$	(33) $O_2^++O \rightarrow O_2+O^+$	(52) $CO+e \rightarrow CO^++e+e$
(16) $H+H+O_2 \rightarrow H_2+O_2$	(34) $O+O \rightarrow O_2^++e$	(53) $O+O+N \rightarrow O_2+N$
(17) $H+H+H_2O \rightarrow H_2+H_2O$	(35) $O+e \rightarrow O^++e+e$	* 'N' stands for Ar, Ar^+, CO_2, CO and H_2
(18) $CH_4+H \rightarrow CH_3+H_2$	(36) $O_2+e \rightarrow O+O+e$	
(19) $CH_3+O_2 \rightarrow CH_2O+OH$	(37) $O_2+e \rightarrow O2^++e+e$	

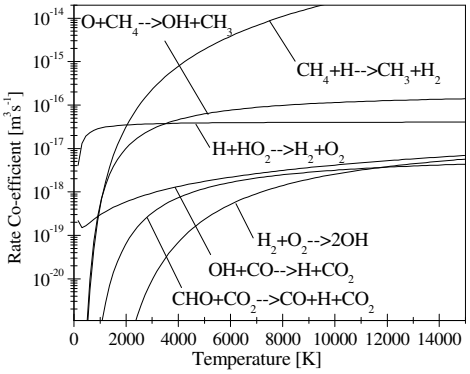

Fig.1. Variation of heavy particle temperature dependent reaction rates with temperature

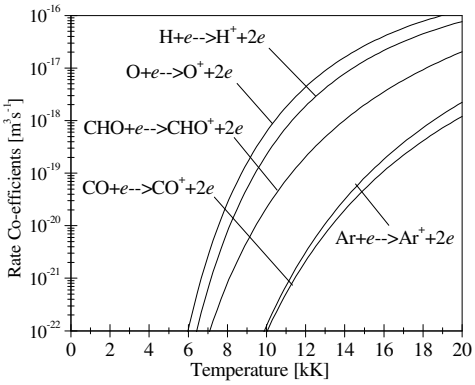

Fig.2. Variation of electron temperature dependent reaction rates as a function of temperature

distribution function, (II) Plasma is axis-symmetric, (III) Plasma is optically thin, (IV) The reaction rates depend on temperature, not directly on electric field strength (V)

3.2 Governing equations and calculation space

Calculation was performed for the high power radio frequency ICTP system setup installed in our laboratory. The schematic configuration with calculation space of the high power ICTP system is shown in Fig. 3 [16]. The governing conservation equations for the non-equilibrium model are as follows:

Mass conservation:

$$\frac{\partial \rho}{\partial t}+\frac{\partial(\rho u)}{\partial z}+\frac{1}{r}\frac{\partial\,(r\rho v)}{\partial r}=0$$

Momentum conservation:

$$\frac{\partial(\rho u)}{\partial t}+\frac{\partial(u\rho u)}{\partial z}+\frac{1}{r}\frac{\partial(rv\rho u)}{\partial r}=$$
$$-\frac{\partial p}{\partial z}+2\frac{\partial}{\partial z}\left(\eta\frac{\partial u}{\partial z}\right)$$
$$+\frac{1}{r}\frac{\partial}{\partial r}\left[\eta r\left(\frac{\partial u}{\partial r}+\frac{\partial v}{\partial z}\right)\right]+\mu_0\sigma\Re\left[\dot{E}_\theta\dot{H}_r\right]$$
$$\frac{\partial(\rho v)}{\partial t}+\frac{\partial(u\rho v)}{\partial z}+\frac{1}{r}\frac{\partial(rv\rho v)}{\partial r}=$$
$$-\frac{\partial p}{\partial r}+\frac{\partial}{\partial z}\left[\eta\left(\frac{\partial v}{\partial z}+\frac{\partial u}{\partial r}\right)\right]$$
$$+\frac{2}{r}\frac{\partial}{\partial r}\left(\eta r\frac{\partial v}{\partial r}\right)-2\eta\frac{v}{r^2}+\mu_0\sigma\Re\left[\dot{E}_\theta\dot{H}_r\right]$$
$$\frac{\partial(\rho w)}{\partial t}+\frac{\partial(u\rho w)}{\partial z}+\frac{1}{r}\frac{\partial(rv\rho w)}{\partial r}=$$
$$\frac{\partial}{\partial z}\left(\frac{\partial w}{\partial z}\right)+\frac{1}{r}\frac{\partial}{\partial r}\left(\eta r\frac{\partial w}{\partial r}\right)-\frac{\rho vw}{r}-\frac{w}{r}\frac{\partial}{\partial r}(r\eta)$$

Translational energy conservation equation:

$$\frac{\partial(\rho h)}{\partial t}+\frac{\partial(u\rho h)}{\partial z}+\frac{1}{r}\frac{\partial(rv\rho h)}{\partial r}=\frac{\partial}{\partial z}\left(\lambda^{tr}\frac{\partial T}{\partial z}\right)$$
$$+\frac{1}{r}\frac{\partial}{\partial r}\left(r\lambda^{tr}\frac{\partial T}{\partial r}\right)+\sum_j\left[\begin{array}{l}\frac{\partial}{\partial z}\left(\rho D_j h_j\frac{\partial Y_j}{\partial z}\right)+\\ \frac{1}{r}\frac{\partial}{\partial r}\left(r\rho D_j h_j\frac{\partial Y_j}{\partial r}\right)\end{array}\right]+\sigma E_\theta E^*{}_\theta-P_{rad}-\sum_{l=1}^{L}\Delta Q_l$$

Mass conservation of species j :

$$\frac{\partial(\rho Y_j)}{\partial t}+\frac{\partial(u\rho Y_j)}{\partial z}+\frac{1}{r}\frac{\partial(rv\rho Y_j)}{\partial r}$$
$$=\frac{\partial}{\partial z}\left(\rho D_j\frac{\partial Y_j}{\partial z}\right)+\frac{1}{r}\frac{\partial}{\partial r}\left(r\rho D_j\frac{\partial Y_j}{\partial r}\right)$$
$$+m_j\sum_{\ell=1}^{L}(\beta_{j\ell}^r-\beta_{j\ell}^f)\left(\alpha_\ell^f\prod_{i=1}^{N}n_i^{\beta_{i\ell}^f}-\alpha_\ell^r\prod_{i=1}^{N}n_i^{\beta_{i\ell}^r}\right)$$

where t : time (s), r : radial position (m), z : axial position (m), u : axial flow velocity (m/s), v : radial flow velocity (m/s), ρ : mass density (kg/m^3), p : pressure (Pa), η : viscosity (Pa.s), h : whole enthalpy (J/kg), h_j : enthalpy of species j (J/kg), T : temperature (K), λ^r : translational thermal conductivity 、 σ : electrical conductivity (s/m), P_{rad} : radiation loss (w/m^3), D_j' effective diffusion coefficient of particle j (m^2/s), x_j : mole fraction of species j, n_j : number density of species j (m^{-3}), Y_j : mass fraction of species j, m_j : mass of species j (kg), $\alpha_\ell^f, \alpha_\ell^r$: rate coefficients of forward and backward reaction ℓ, $\beta_{j\ell}^f, \beta_{j\ell}^r$: stoichiometric number of species j in forward and backward reaction ℓ, μ_0 : permeability of vacuum (h/m), κ : Boltzmann constant (J/k), $\dot{E}_\theta$: electric field strength (v/m), $\dot{H}_r$: radial magnetic field strength (a/m), ΔQ_l reaction heat per unit volume and time (J/s/m^2), N : total number of species, L : total number of reactions

We solved mass, momentum, energy conservation equations, Maxwell equations for vector potential and also mass conservation equations for each species. In one-temperature condition, energy conservation equations for heavy particles and electrons should be considered in the same equations. Enthalpy flow caused by diffusion had been treated explicitly in the energy conservation equation. Chemical non-equilibrium was considered by taking the actual reaction rates which substantially affect the mass fraction term of each species, reaction heat per unit volume and time and thus the effective diffusion coefficient. This consideration eventually affects the enthalpy flow caused by diffusion.

Thermodynamic and transport properties were calculated at each position using the cross-section data and the locally calculated particle composition and the temperature by the first order approximation of Chapman-Enskog method. The gas flow is laminar. Turbulence flow has been neglected. The pressure was set to atmospheric pressure. Total sheath gas flow rate is set to 100 slpm (standard liter per minute). Input power to the plasma is fixed at 27 kW and was set at a radio frequency of 450 kHz.

Fig.4 shows the calculation domain where O-A-B-C-D-E-F is the calculation space inside which fluid parameters and scalar quantities were evaluated. The two-dimensional space co-ordinate are O (0, 0), A (0, 35), B (330, 35), C (330, 65), D (480, 65), E (910, 20) and F (910, 0) where the unit is in mm. The inner diameter at the plasma torch and reaction chamber (downstream) was 70 mm and 130 mm respectively. The numerical calculation was carried out using SIMPLE algorithm with uniform grid system having 66 radial and 92 axial nodes.

3.3 Results and discussion for chemically non-equilibrium model

3.3.1 Temperature distribution

Fig.5 shows the temperature distribution of 98%Ar-1%CO_2-1%H_2 plasma at atmospheric pressure for (a) one temperature non chemical equilibrium condition (1T-NCE) and (b) one temperature chemical equilibrium condition, i.e. LTE condition. The resultant maximum temperature reaches near 10000 K in this torch for both cases. As seen, there is a smaller region with temperatures above 10000 K for 1T-NCE results compared to that for LTE result. Fig.6 shows the radial temperature distributions at an axial position of 155 mm for the two cases and it suggests that considering non chemical equilibrium effect in calculation causes wider plasma or relatively flatter distribution than 1T-CE mainly for taking diffusion terms into account. This is because diffusion of electrons causes planer electron density distribution and so is the electrical conductivity distribution. This relatively planer electrical conductivity distribution gives rise to scattered joule heating dissipation.

3.3.2 Particle density distribution

Fig.7 represents mass fraction distribution of Ar, Ar^+, H^+ and electrons as an example in the same plasma by the 1T-NCE model. These mass fraction profiles demonstrate that ionized particles and electrons tend to accumulate at the plasma torch region that makes high temperature area electrically conductive.

Fig.8 (a) depicts radial distributions of particle composition at an axial position of 155 mm calculated by 1T-NCE model. Estimation of actual reaction rates and consideration of convection and diffusion terms markedly affect the particle distributions. CO_2 and H_2 molecules are dissociated into CO, O, H and other atoms at the plasma torch. Ionizations for various particles also occur at the high temperature plasma region though electrons are mainly produced by Ar ionization. Near the torch wall, many kinds of molecules such as CH_2O, H_2O and H_2 are produced by association of atoms. Fig.8 (b) illustrates that of 1T-CE model at the same position. For comparison, at the region of r<20 mm, it has been found for NCE model that number density of CO_2 is much higher than that of CE model which suggests that NCE model considers much lower dissociation of CO_2. On the other hand, association of atoms such as CH_4 is much higher in CE model near the wall.

At the region of r=20-25mm, for CE calculation, density curves for the ionized particles sharply fall lower values as we go from core to peripheral region. But in NCE calculation, these curves are relatively flatter which implies that ionization reactions are concentrated inside the core of plasma for chemical equilibrium condition because the diffusion is not taken into account.

In NCE calculation, diffusion of electrons easily occurs as electron has a very light mass. Then due to ambipolar diffusion, positive ions are attracted to the outer periphery. For neutral atoms, we see relatively flatter rising curves towards the peripheral region for NCE calculation.

3.4 Experimental

Experiment was performed for the same ICTP system setup. The setup comprises of two basic parts namely (a) plasma torch and (b) reaction chamber. The plasma torch portion is made up with two coaxial quartz tubes of 3.0 mm thickness. Between the gaps of the tubes, cooling water at room temperature flows for efficient cooling of tube wall. The inner diameter and length of plasma torch are 70 mm and 330 mm respectively. Along the inside tube wall, pure Ar and Ar-CO_2+H_2 gas mixture is supplied as a sheath gas. A winding of eight turn induction coil is installed around the plasma torch.

The observation position is adjusted to 10 mm below the coil end on the central axis. The light radiated from the observation point was transmitted through an optical filter, camera lens, a mirror, and an optical fiber bundle to the slit of a monochromator. A one-dimensional multi channel detector was installed at the focal plane of the monochromator to measure the light intensities at the range of 100 nm simultaneously with a resolution of 0.3 nm.

Fig.9 (a) and (b) illustrate the photograph taken by high speed digital video camera and radial distributions of radiation intensity at 10 mm below the coil end. The figure suggests that inclusion of CO_2 and H_2 mixture into pure Ar causes the plasma shrinkage due to the fact that CO_2 and H_2 mixture has relatively higher specific heat and thermal conductivity than that of Ar which results better convection and conduction of heat from plasma core to peripheral region. The important observation from this experimental result is the shrinkage of plasma due to inclusion of CO_2 and H_2 molecular gas mixture.

4. Conclusions

Estimation of dominant particles and reactions were made for chemically non-equilibrium modeling of Ar-$C_xH_yO_z$ plasma for high power density plasma-assisted combustion system and observation of pressure variation has been done. This report of numerical modeling of Ar thermal plasma with $C_xH_yO_z$ molecular gas system will play an undoubtedly important role in predicting the plasma assisted combustion process field where chemically non-equilibrium effect has been taken into account.

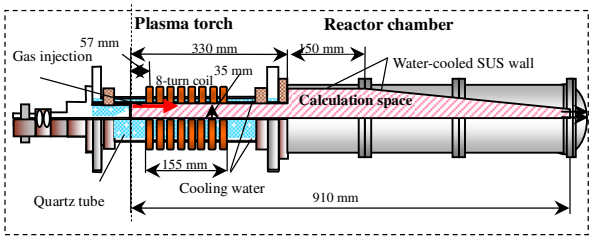

Fig.3 Plasma torch configuration

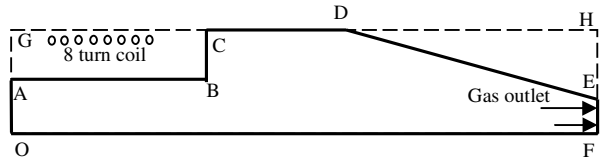

Fig.4 Calculation domain

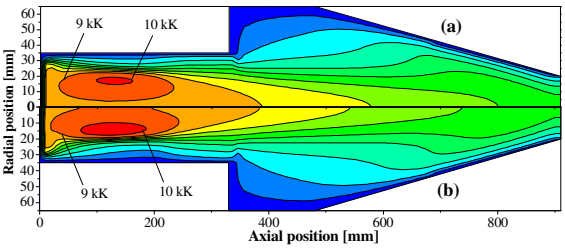

Fig.5 Two-dimensional temperature distribution of 98%Ar-1%CO_2-1%H_2 plasmas at (a)1T-NCE, (b)1T-CE condition

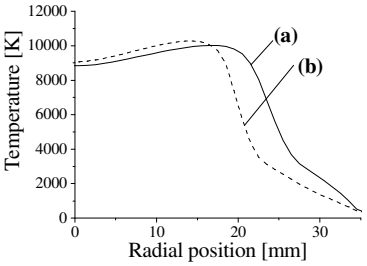

Fig.6 Radial temperature distribution for (a) 1T-NCE and (b) 1T-CE condition at an axial position of 155 mm

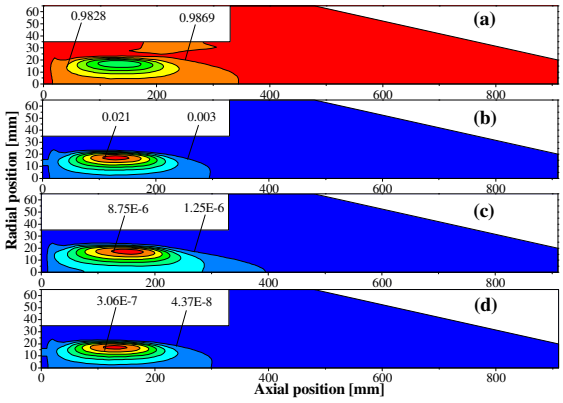

Fig.7 Two-dimensional mass fraction distributions for (a) Ar, (b) Ar+, (c) H+ and (d) electron for 1T-NCE condition

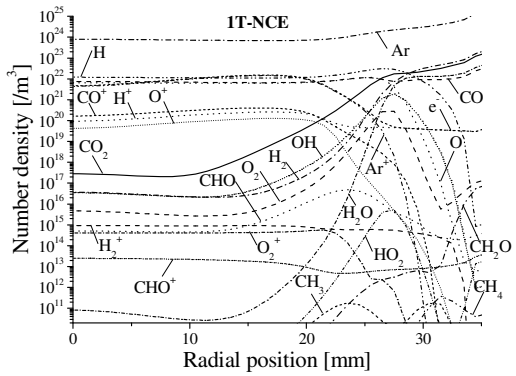

Fig.8 (a) Radial distributions of particle composition at an axial position of 155 mm for 1T-NCE condition

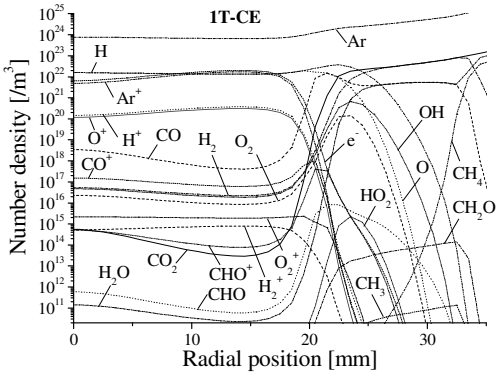

Fig.8 (b) Radial distributions of particle composition at an axial position of 155 mm for 1T-CE condition

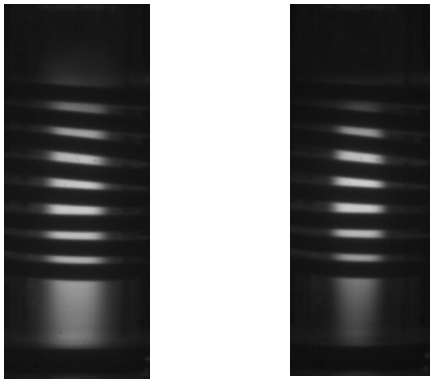

(a)(I) (a) (II)

Fig.9 (a) Snapshots taken from high speed video camera for (I) Ar-100slpm and (II) 98%Ar-1%CO_2-1%H_2

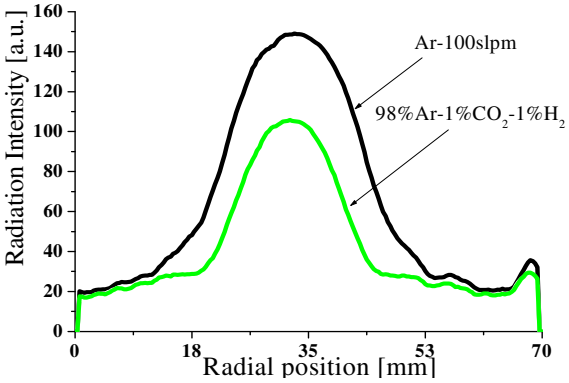

Fig.9 (b) Radial distribution of radiation intensity at 10 mm below the coil end for two cases

5. References

[1] Maher I. Boulos, *et al*., THERMAL PLASMAS Fundamentals and Applications, vol. 1, *Springer*, Plenm Press New York, 1994

[2] Al-Mamun *et al*., *IEEJ Trans. PE*, Vol. 128, No. 2, 2008, pp.479-485

[3] M. W. Chase, *et al*., *JANAF thermodynamical tables*, 3rd edn., NSRDS, vol. 14 , 1985

[4] T.Takagi, *et al.*, Analysis of Complex Flows, University of Tokyo Press, ISBN 4-13-065105-6, 1995

[5] http://physics.nist.gov/PhysRefData/Ionization/atom_index.html

[6] T. G. Owano, *et al.*, *AIAA*, vol. 31, p.75-82, 1993

[7] A.V. Phelps, *et al*., *J. Phys. Chem. Ref. Data*, vol.20, p.557-573, 1991

[8] Y. Tanaka, *et al*., *Plasma Sources Sci. Technol.* 14, p.134-151, 2005

[9] http://vulcan-cfd.larc.nasa.gov

[10] http://www.chemeng.ucl.ac.uk/research/combustion/thesis/append3.html

[11] Murrel and Rodriguez *et al*. 1986

[12] Miller and Melius *et al*. 1992

[13] Colket *et al*. 1986

[14] Zhang and McKinnon *et al*. 1995

[15] Tsang and Hampson *et al*. 1986

[16] Y.Tanaka:, *J. Phys. D: Appl. Phys.*, 37, pp. 1190-1205, 2004